HHS Public Access

Author manuscript

Mol Cell. Author manuscript; available in PMC 2023 August 04.

Published in final edited form as:

Mol Cell. 2022 August 04; 82(15): 2832–2843.e7. doi:10.1016/j.molcel.2022.05.024.

Metabolic-scale gene activation screens identify SLCO2B1 as a heme transporter that enhances cellular iron availability

Gokhan Unlu[1], **Benjamin Prizer**[1], **Ranya Erdal**[1,2], **Hsi-Wen Yeh**[1], **Erol C. Bayraktar**[1,†], **Kıvanç Birsoy**[1,*]

[1]Laboratory of Metabolic Regulation and Genetics, The Rockefeller University, New York, NY 10065, USA

[2]Medical Scientist Training Program, Hacettepe University Faculty of Medicine, Ankara 06230, Turkey

SUMMARY

Iron is the most abundant transition metal essential for numerous cellular processes. While most mammalian cells acquire iron through transferrin receptor, molecular players of iron utilization under iron-restriction are incompletely understood. To address this, we performed metabolism-focused CRISPRa gain-of-function screens, which revealed metabolic limitations under stress conditions. Iron restriction screens identified expected members of iron utilization pathways, but also *SLCO2B1* a poorly characterized membrane carrier. *SLCO2B1* expression is sufficient to increase intracellular iron, bypass the essentiality of transferrin receptor and enable proliferation under iron restriction. Mechanistically, SLCO2B1 mediates heme-analog import in cellular assays. Heme uptake by SLCO2B1 provides sufficient iron for proliferation through heme oxygenases. Notably, *SLCO2B1* is predominantly expressed in microglia in the brain and primary *Slco2b1*$^{-/-}$ microglia mice exhibit strong defects in heme-analog import. Altogether, our work identifies SLCO2B1 as a microglia-enriched plasma membrane heme importer and provides a genetic platform to identify metabolic limitations under stress conditions.

Graphical Abstract

*Corresponding and Lead Contact: kbirsoy@rockefeller.edu.

†Present address: Department of Pathology, New York University School of Medicine, New York, NY 10016, USA

AUTHOR CONTRIBUTIONS

Conceptualization, K.B. and G.U.; Methodology, G.U. and K.B.; Formal Analysis, G.U.; Investigation, G.U., B.P., R.E., H.-W.Y and E.C.B; Writing – Original Draft, G.U. and K.B.; Funding Acquisition, K.B. and G.U.

DECLARATION OF INTERESTS

K.B. is scientific advisor to Nanocare Pharmaceuticals and Barer Institute. Other authors declare no competing interests.

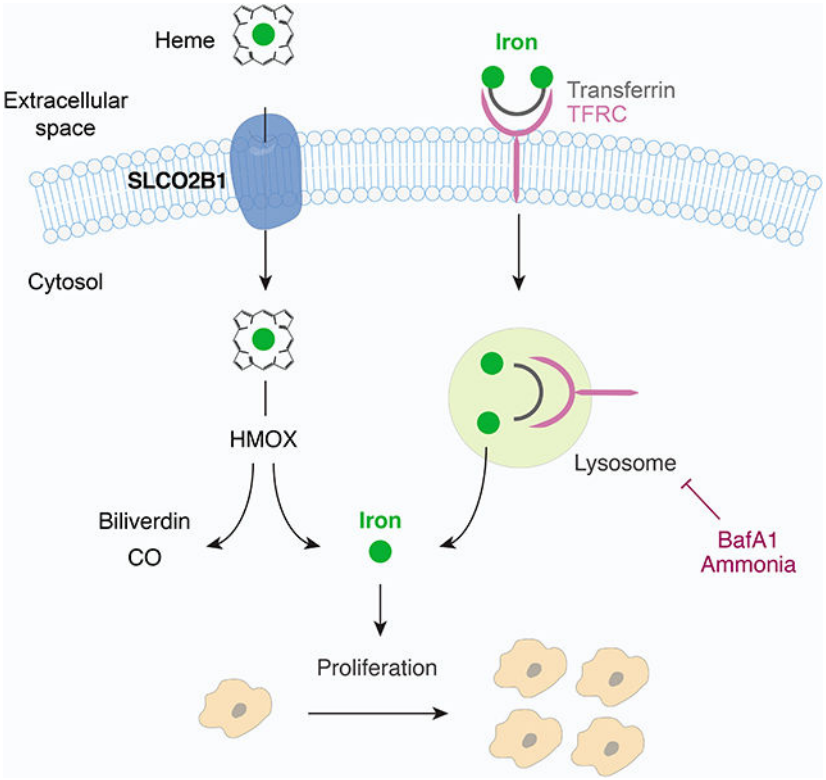

eTOC blurb

Unlu et al. perform metabolism scale CRISPRa screens to reveal metabolic limitations under stress conditions. Focusing on iron restriction, they identify *SLCO2B1* as a plasma membrane heme carrier that increases cellular iron availability independently of *TFRC*. *SLCO2B1* is enriched in microglia in the brain and required for heme-analog import.

INTRODUCTION

Iron is the most abundant transition metal and essential for almost all living species. A significant fraction (2%) of human proteins binds to iron in the form of heme (iron-protoporphyrin IX), iron-sulfur (Fe-S) clusters, and as free ion (Andreini et al., 2018; Kaplan and Ward, 2013). Owing to its unique redox characteristics, iron mediates a wide range of biological process including oxidative phosphorylation, DNA replication and antioxidant response. In mammals, iron deficiency causes anemia but is also associated with impaired neurological function and weakened immune response (Jiang et al., 2019; Yager and Hartfield, 2002). In contrast, excess cellular iron generates reactive oxygen species that damage cellular macromolecules, and is linked to aging, liver failure and neurodegeneration (Sato et al., 2022; Wang et al., 2017). Most mammalian cells take up iron in the form of transferrin, a serum glycoprotein that maintains it in soluble form and limits the generation of free radicals. However, iron also associates with other carriers in the serum such as ferritin, heme and albumin. These carriers are particularly critical under disease conditions where transferrin-bound iron levels are limiting (Leitner and Connor, 2012; Moos and

Morgan, 1998). However, molecular players involved in iron utilization under iron-restricted conditions are incompletely understood.

To address this, we developed a metabolic scale CRISPR activation (CRISPRa) screening platform and performed gain-of-function genetic screens under iron-limiting conditions. These screens revealed multiple mechanisms that enable cell proliferation under iron restriction. Our work also identified *SLCO2B1*, a poorly characterized plasma membrane transporter, as a heme transporter that promotes cellular iron availability. *SLCO2B1* is predominantly expressed in microglia in the brain and primary microglia from *Slco2b1*$^{-/-}$ mice exhibit a strong defect in heme analog import. Our results reveal metabolic limitations under iron restriction and identify a plasma membrane heme transporter in microglia.

RESULTS

Metabolic-scale gene activation screens identify metabolic processes limiting for cell proliferation under iron restriction

One approach to identify metabolic limitations under stress is to systematically induce the expression of small molecule transporters and enzymes and determine those that restore cell proliferation in response to a particular stress. Activation of target gene expression can be achieved with nuclease dead Cas9 (dCas9a) fused to a transcriptional activator (VP64-p65-Rta). Using this technology, we generated a metabolism focused sgRNA library consisting of 32,509 sgRNAs that target 2989 metabolic enzymes and small molecule transporters (Figure 1A, Table S1). To test the robustness of the approach, we first performed gain-of-function genetic screens in dCas9a expressing PaTu-8988t pancreatic cancer cells (Figure S1A) treated with near-lethal doses of several metabolic inhibitors. These small molecules include Antimycin A, an electron transport chain (ETC) inhibitor, CB-839, an inhibitor of glutaminolysis, buthionine sulfoximine (BSO), an inhibitor of glutathione synthesis, and palmitate, a saturated fatty acid that disrupts membrane lipid homeostasis at high levels. After selection with these agents, we harvested DNA from surviving cell populations and calculated the percentage of total sgRNA reads mapping to each gene. Genes with highest percentage sgRNA reads protect cells from the corresponding toxic agents and reveal potential metabolic limitations for cell proliferation under these stress conditions.

Among the scoring genes that protect cells against ETC inhibition are *SLC1A1* and *SLC1A3*, both of which are aspartate/glutamate plasma membrane transporters and increase aspartate import from the culture media. Indeed, previous work has determined that aspartate is a limiting metabolite for cancer cell proliferation under ETC inhibition (Birsoy et al., 2015) (Figures 1B and S1B). Interestingly, our screens also identified *ASRGL1*, a putative human L-asparaginase, which catalyzes the deamidation of asparagine to produce aspartate. While ASRGL1 has previously been shown not to display amidase activity at physiological levels of expression (Pavlova et al., 2018), our data suggest that ASRGL1 may synthesize meaningful levels of aspartate when overexpressed in human cells. Conferring resistance to CB-839, our screens identify *GLS2*, a paralog of *GLS1*, as a gene that can bypass GLS1 inhibition, supporting the selective on-target effect of CB-839 on GLS1 (Figures 1C, S1C). *SLC1A1/3* and *ASRGL1* also scored likely due to their ability increase the cellular levels of glutamate, a limiting metabolite for TCA cycle progression under glutaminase

inhibition. In line with the fact that BSO is a competitive glutamate analog (Meister, 1995), the only scoring gene in the BSO screen was glutamate—cysteine ligase catalytic subunit (GCLC), which catalyzes the first enzymatic step in glutathione (GSH) synthesis (Figures 1D and S1D). Finally, expression of *FADS2* (fatty acid desaturase) and *SCD* (stearoyl-CoA desaturase), the two enzymes involved in fatty acid desaturation, protect cells against lipid saturation stress upon palmitate treatment (Figures 1E and S1E). Additional hits conferring resistance to palmitate were *FADS1*, which introduces *cis* Δ5 double bond during polyunsaturated fatty acid (PUFA) synthesis (Cho et al., 1999); *ACSL4* ,the major enzyme that produces long chain PUFA containing lipids, *ADIPOR2*, which acts as a sensor for membrane fluidity and *SLCO4A1*, an uncharacterized transporter (Devkota et al., 2017; Ruiz et al., 2019) (Figure S1F). Notably, *SLCO4A1* has previously been shown to be coessential with enzymes in fatty acid metabolism, indicating its potential role in membrane lipid homeostasis (Aregger et al., 2020). These results highlight the utility of metabolism-scale gain of function screens to discover potential metabolic limitations under stress conditions.

We next sought to use this platform as a discovery tool to identify cellular pathways that regulate cellular iron availability under iron restriction. While iron chelators are commonly used to deplete cellular iron, we recently showed that disrupting endosomal and lysosomal acidity also decreases cellular iron levels by hindering transferrin-mediated iron import (Weber et al., 2020). We therefore performed positive selection CRISPRa screens in Jurkat dCas9a cells (Figure S1A) and determined genes whose expression would overcome anti-proliferative effects of iron restriction induced by an iron chelator, deferoxamine mesylate (DFO, 2 μM), and an endo-lysosomal pH inhibitor, Bafilomycin A1 (BafA1, 5 nM) (Figures 2A and 2B). Scoring genes should identify metabolic limitations under iron depletion and reveal alternative pathways involved in iron acquisition. Consistent with the observation that DFO and BafA1 impair cell proliferation via distinct mechanisms, most of the scoring genes were unique to each condition. Among the scoring genes in DFO screens are *SLC25A37* and *SLC25A28*, mitochondrial iron importers (Shaw et al., 2006). Additionally, plasma membrane and endosomal ferric reductases that reduce Fe^{3+} to Fe^{2+} also scored, including *CYBRD1*, *FRRS1* and *CYB561A3* (Figure 2C) (Vargas et al., 2003; Wang et al., 2021). In contrast, genes conferring resistance to BafA1 included v-ATPase subunits *ATP6V0A2* and *ATPV1E1* among the top hits. These subunits are adjacent to the BafA1 binding site on the v-ATPase, and their overexpression likely blocks inhibition of v-ATPase activity by BafA1 (Figure 2D and 2E).

Iron plays essential roles in different compartments in cells. In addition to proteins containing heme or iron-sulfur (Fe-S) clusters, whose syntheses occur in the mitochondrial matrix, there are other key enzymes containing iron, but devoid of Fe-S clusters or heme. For example, di-iron center is present in a group of non-mitochondrial enzymes such as ribonucleotide reductases, oxygenases and fatty acid desaturases (Bollinger Jr et al., 1991; Ryle and Hausinger, 2002; Shen et al., 2020). Given that both mitochondrial iron transporters scored in our genetic screens, we hypothesized that iron availability in mitochondria, but not in the cytosol or other organelles, is the limiting process for cell proliferation under environmental iron restriction. Consistent with this hypothesis, overexpression of either mitochondrial iron transporter *SLC25A37* or *SLC25A28* was

sufficient to sustain cell proliferation at lethal DFO concentrations (Figures 2F, 2G and S1G). These data suggest that mitochondrial iron availability is the limiting process for proliferation when cells are deprived of iron. Altogether, our screens identify distinct metabolic players involved in cell survival and proliferation under iron chelation and lysosomal pH inhibition. Strikingly, *SLCO2B1*, a poorly characterized small molecule transporter, was the only common hit upon DFO and BafA1-induced iron restriction (Figures 2C, 2D, S2A, S2B and S2C). We therefore focused our attention on it.

SLCO2B1 expression is sufficient to sustain cell proliferation under iron restriction

SLCO2B1 is a member of organic anion transporter family (König, 2011) and has previously been shown to transport a multitude of drugs and steroid hormone conjugates (Grube et al., 2006; Medwid et al., 2019). However, its precise physiological substrate and relevance to iron metabolism is unknown. To begin to study its function, we generated a Jurkat cell line that expresses *SLCO2B1* cDNA (Figure S2D). Consistent with the screen results, cells expressing *SLCO2B1* can proliferate even under lethal doses of DFO and BafA1, in contrast to those expressing a control vector, its closely related paralog *SLCO2A1* or a short *SLCO2B1* isoform (Figures 3A, 3B, S2E, S2F). This finding is generalizable to other cell lines, as *SLCO2B1* expression in PaTu-8988t cells protected them from DFO and BafA1-induced toxicity (Figures S2G and S2H). Additionally, positive selection CRISPRa screens in a mouse pancreas cancer cell line identified *Slco2b1* as the top protective gene against lysosomal pH dysfunction (Figures S2I, S2J, S2K, S2L and S2M; Table S2). Iron supplementation diminished the proliferation difference between control and *SLCO2B1*-expressing cells growing in otherwise lethal dose of BafA1 (Figure 2**N**). Furthermore, *SLCO2B1*-overexpressing cells displayed similar resistance to deferiprone (DFP), a lipid-soluble iron chelator, v-ATPase inhibitor concanamycin (ConA) and NH_4Cl, which disrupts lysosomal acidity by acting as a lysosomotropic weak base (Klempner and Styrt, 1983) (Figures 3C, 3D and 3E). These findings reveal that *SLCO2B1* expression is sufficient to sustain proliferation of mammalian cells under different modes of iron depletion.

SLCO2B1 promotes iron availability, independently of transferrin-mediated iron uptake in mammalian cells

We next sought to determine the role of *SLCO2B1* in cellular iron metabolism. To address this in an unbiased way, we profiled cellular metabolites from Jurkat cells expressing *SLCO2A1* (control) or *SLCO2B1* cDNA by liquid chromatography-mass spectrometry (LC-MS). However, only few metabolites change in response to *SLCO2B1* overexpression, suggesting that *SLCO2B1* expression does not cause a strong change in the levels of cellular metabolites (Figures S3A and S3B). Cellular iron homeostasis is tightly controlled in cells by a post-translational mechanism mediated by IRP1/2 pathway (Sviderskiy et al., 2019). An increase in iron levels negatively regulate IRP2, enhancing mRNA stability of ferritin heavy chain 1 (FTH1), the major iron storage protein in mammalian cells. To test whether *SLCO2B1* modulates iron homeostasis, we determined IRP2 and FTH1 protein levels in cells expressing *SLCO2B1*. Expression of *SLCO2B1* caused a marked induction in the protein levels of FTH1 across several mammalian cell lines tested, under standard culture conditions (Figures 3F and S3C). We next asked whether *SLCO2B1*-expressing cells maintain higher levels of iron stores even under iron restriction. Indeed, expression of

SLCO2B1 strongly blocked the increase in IRP2 and the decrease in FTH1 protein levels in response to treatment with lysosomal pH inhibitors (Figure 3G). Finally, to directly measure iron levels in these cells, we conducted inductively coupled plasma mass spectrometry (ICP/MS) measurements. Consistent with the increase in ferritin levels, iron levels in *SLCO2B1*-expressing cells were ~2-fold higher than those of the parental controls. Notably, we did not observe any significant change in the levels of other divalent metals (Cu, Mn and Zn), indicating a specific effect of SLCO2B1 on iron homeostasis (Figure 3H). These results suggest that SLC2OB1 regulates the iron response pathway by increasing cellular iron stores.

Under physiological conditions, TFRC-mediated iron uptake is the main route of iron acquisition (Richardson and Ponka, 1997). Indeed, *TFRC* is a universally essential gene for the proliferation of most cell lines (Tsherniak et al., 2017). To determine whether *SLCO2B1* expression bypasses the requirement of TFRC-mediated iron uptake, we knocked out *TFRC* by CRISPR/Cas9 in Jurkat cells expressing *SLCO2B1*, its paralog *SLCO2A1* or vector control (Figure S3D). Consistent with the essential function of *TFRC* for cell survival, parental Jurkat cells and those expressing *SLC2OA1* died upon its depletion. Supplementation of culture media with excess free iron, i.e., ferric iron citrate (FAC), was sufficient to restore cell proliferation. In contrast, *SLCO2B1* expression in Jurkat cells completely restored their survival and proliferation in response to *TFRC* loss even in the absence of iron supplementation (Figures 3I and 3J). These results strongly suggest that *SLCO2B1* promotes iron availability and cell proliferation under iron restriction, independently of transferrin-mediated iron uptake.

Heme oxygenase is essential for SLCO2B1-induced resistance to iron restriction

To understand how *SLCO2B1* expression enables cell survival under iron restriction, we performed a negative selection CRISPR screen in parental Jurkat cells and those expressing *SLCO2B1*, treated with a normally lethal dose of BafA1. These screens should identify metabolic processes required for *SLCO2B1*-mediated rescue of iron restriction. Additionally, given that *SLCO2B1*-expressing cells tolerate high levels of BafA1 treatment, this provides a unique opportunity to determine metabolic processes that enable cell proliferation under severe lysosomal dysfunction (Figures 4A, 4B, S4A and S4B). Indeed, among the scoring genes differentially essential under lysosomal pH inhibition are those involved in cholesterol (*LSS, SREBF2*, *ACAT2*, *SQLE*, *FDFT1*) and sphingolipid (*SPTLC1*, *SPTLC2* and *SGMS1*) biosynthesis. Cholesterol and sphingolipids can be synthesized *de novo*, but also acquired from extracellular lipoproteins through lysosomal enzymes (Goldstein and Brown, 2009; Levade et al., 1996). Similarly, cysteine import into lysosomes requires the lysosomal pH gradient. Likely due to the decrease in lysosomal cysteine storage, cells become dependent on cystine uptake mediated by SLC7A11 (Figures 4C and S4B) (Pisoni et al., 1990). Further work is needed to determine why several other processes scored as conditionally essential and how they may compensate for lysosomal dysfunction in mammalian cells.

Interestingly, the only scoring gene relevant to iron metabolism and differentially essential in *SLCO2B1* expressing cells was *HMOX2*, a heme oxygenase (HMOX) required for heme

degradation (Figures 4B, 4C, 4D and S4A). HMOX enzymes break down the porphyrin ring of heme to produce biliverdin, carbon monoxide and iron. Notably, while most mammalian cells express two HMOX paralogs, HMOX2 is the predominantly expressed one in Jurkat cells (TPM of HMOX1 = 0.3, HMOX2 = 32.8, DepMap portal). To test whether *HMOX2* is necessary for SLCO2B1-mediated resistance against iron restriction, we deleted *HMOX2* in parental and *SLCO2A1* or *SLCO2B1*-expressing Jurkat cells. Consistent with the screen results, *HMOX2* loss completely abolished *SLCO2B1*-mediated resistance to BafA1 and DFO treatment (Figures 4E, 4F and S4C). Given the requirement of *HMOX2* for *SLCO2B1*-mediated resistance, we reasoned that *HMOX2* loss would block the increase in iron availability and the corresponding decrease in IRP2 protein abundance of *SLCO2B1* expressing cells. In line with our model, *HMOX2* loss restored IRP2 protein levels in SLCO2B1-expressing cells (Figure 4G). Collectively, these results suggest that HMOX2 acts downstream of SLCO2B1 to increase intracellular iron availability.

Given that heme degradation is required for SLC2OB1 function, we next sought to determine whether SLCO2B1 is involved in heme metabolism. Interestingly, when we compared gene essentialities between parental cells and those expressing *SLCO2B1*, we found that *UROD* (uroporphyrinogen decarboxylase), like *TFRC*, is essential only in parental cells and not in *SLCO2B1* expressing counterparts (Figures 4H, 4I, S4E, S4F). UROD is a universally essential enzyme in mammalian cells and catalyzes the third step of heme biosynthesis in the cytosol. We therefore asked whether *SLCO2B1* expression may bypass the dependence of mammalian cells on *de novo* heme synthesis. While loss of *UROD* blocked the proliferation of parental Jurkat cells, expression of *SLCO2B1* completely eliminated the anti-proliferative effects of *UROD* depletion (Figure 4J). Protein levels of ALAS1, the rate limiting enzyme of heme synthesis, is negatively regulated by cellular heme levels. In line with this, expression of *SLCO2B1*, but not control cDNAs, reduced the increase in ALAS1 protein levels in response to UROD depletion (Figure 4K and S4G). Similarly, *SLC2OB1* expression blocked the increase in ALAS1 levels in cells treated with succinyl acetone, the pharmacological inhibitor of heme synthesis (Figures S4D and S4H). Altogether, these results indicate that *SLCO2B1* expression is sufficient to restore cell proliferation in cells deficient for heme synthesis enzyme, UROD.

SLCO2B1 expression is necessary and sufficient for the uptake of heme analogs

SLCO2B1-expressing cells are remarkably resistant to the effects of iron restriction and heme synthesis deficiency, suggesting that SLCO2B1 may be a potential heme importer. To first determine the localization of SLCO2B1, we expressed in PaTu-8988t cells a C-terminally eGFP-tagged version of SLCO2B1, which is comparably functional to restore cell viability upon BafA1 treatment (Figures S5A, S5B, S5C and S5D). Confocal microscopy analysis of the SLCO2B1-eGFP fusion protein showed a strong plasma membrane localization (Figure S5A). To quantitatively measure steady state heme uptake, we used Zinc mesoporphyrin (ZnMP), a fluorescent heme analog (Figure 5A). We treated cells with ZnMP and measured intracellular fluorescence by flow cytometry. ZnMP uptake was markedly higher in *SLCO2B1*-expressing cells across three human cell lines tested (Jurkat 24h uptake; HepG2 and PaTu-8988t 15 min uptake assays) compared to parental controls (Figures 5B, 5C and 5D). To formally prove the direct cellular uptake, we next performed a ZnMP uptake

assay in a time- and dose-dependent manner. During a 15-min dose-dependent uptake assay, *Slco2b1*-expressing cells took up significantly more ZnMP at all doses tested (e.g. >5 fold at 0.5 μM) (Figures 5E, 5F and S5E). Finally, since heme is a highly redox-active molecule, excess uptake of heme should be more toxic to cells that import it more efficiently. We therefore assayed sensitivity of SLCO2B1-expression and control cells to Hemin, a hemelike porphyrin structure with a ferric chloride center (Figure 5G). Indeed, *SLCO2B1* expressing Jurkat cells displayed slower proliferation rates than control and *SLCO2A1*-expressing cells, in response to hemin treatment (Figure 5H). Remarkably, upon hemin addition, *SLCO2B1*-expressing cell pellets, in contrast to controls, displayed a discernably brown color, characteristic of hemin accumulation and greater reduction of ALAS1 (Figure 5I and J). In parallel, *SLCO2B1*-overexpressing cells treated with succinyl acetone upregulated ALAS1 protein levels to a lesser degree than that of control cells, indicating higher heme availability. These results suggest that SLCO2B1 is sufficient for the transport of heme analogs.

We next sought to test whether *SLCO2B1* is necessary for heme analog import. Notably, most cultured mammalian cells we have tested did not exhibit appreciable levels of SLCO2B1 expression. We therefore analyzed a publicly available single cell transcriptome dataset (Tabula Muris Consortium, 2018) to identify cell types with highest *Slco2b1* expression (Figure 6A). Strikingly, *Slco2b1* expression displays a highly restricted expression pattern in microglial cells in brain. To study loss of function of *Slco2b1*, we therefore generated a full body *Slco2b1*-null mouse model (Figure S5F). These knockout mice are viable and enabled us to test the necessity of *Slco2b1* for heme analog uptake in isolated microglial cells (Ledo et al., 2020) (Figure 6B). Cells dissociated from brain, other than microglia, did not display detectable ZnMP positivity (Figures 6C and 6D), suggesting that microglial cells could indeed be the predominant cell type with heme uptake activity in the brain. Remarkably, this ZnMP uptake activity in wild type microglia almost exclusively depends on *Slco2b1* expression. Indeed, microglia from *Slco2b1* knockout mice display a strong reduction in ZnMP import compared to those from wild type controls (i.e., 86% of wild type microglia, as opposed to 2.23% Slco2b1-null microglia, were ZnMP+) (Figure 6E). These results suggest that *Slco2b1* is necessary for heme analog uptake in microglia. Finally, to determine whether *Sloc2b1* loss leads to any physiological changes in microglia, we performed RNA-seq analysis on sorted microglia from adult *Slco2b1*−/− mice and their wild type littermates. Gene ontology (GO) enrichment analysis of upregulated genes in *Slco2b1*−/− microglia revealed inflammation-related GO terms ‘innate immune response’ and ‘cellular response to cytokine-stimulus’ signatures (Figure 6G, H). Notably, *Apoe* and *Clec7a* were amongst the most upregulated genes (Figure 6G; Table S3), which have been implicated in disease-associated microglia during Alzheimer progression and neuroinflammation (Krasemann et al., 2017; Lanfranco et al., 2021). Future studies will determine whether these phenotypes are linked to heme uptake deficiencies in microglia.

DISCUSSION

Proliferating cells commonly experience nutrient limitations due to environmental metabolic stress conditions. This is particularly relevant for tumor cells, where they frequently starve for nutrients due to hypoxia and poor vascularization. Previous work has shown that,

under defined metabolic stressors, supplementation of a single metabolite has the potential to overcome metabolic bottlenecks (Birsoy et al., 2015; Garcia-Bermudez et al., 2018; Possemato et al., 2011). Here, we devised a metabolic-scale gain-of-function screening platform to identify these metabolic bottlenecks. This platform can be readily applied to study metabolic characteristics of diverse tumor models, and to determine limiting metabolic processes for cell growth in culture as well as *in vivo*. A major outcome of our study is the identification of SLCO2B1 as a plasma membrane transporter that mediates heme import. SLCO2B1-mediated heme uptake bypasses two essential metabolic processes in mammalian cells: TFRC-mediated iron uptake and heme biosynthesis. Similar to SLCO2B1, heme uptake by the heme-responsive paralogs, *hrg-1* and *hrg-4*, has extensively been studied in the context of heme-auxotrophic *C. elegans*. Mammalian homolog of *hrg-1* facilitates lysosomal export of heme in splenic macrophages (Rajagopal et al., 2008; White et al., 2013) and *hrg-4* in worms lacks a mammalian homolog. Furthermore, while previous work proposed FLVCR2 as a plasma membrane heme transporter, its ectopic expression failed to rescue heme-deficiency (Chambers et al., 2021; Duffy et al., 2010). Notably, single cell transcriptomics data revealed that *SLCO2B1* expression is highly enriched in microglia (Cao et al., 2020; Tabula Muris Consortium, 2018), indicating that SLCO2B1 might mediate microglial heme import. As free heme levels increase in disease conditions like hematoma and intracranial hemorrhage (Mracsko and Veltkamp, 2014; Vasconcellos et al., 2021), microglial heme uptake by SLCO2B1 could be a defense mechanism to protect neurons and astrocytes from oxidative heme damage. Furthermore, heme uptake may also be relevant in the context of neurodegenerative diseases, as induced *HMOX1* expression and iron accumulation in microglial cells have been observed in Alzheimer's and Parkinson's disease (Fernández-Mendívil et al., 2021; Kenkhuis et al., 2021). Given that neuroinflammation markers, *Apoe* and *Clec7a,* are highly upregulated in *Slco2b1*−/− microglia, it is conceivable that *Slco2b1* knockouts might be more susceptible to neurodegeneration and neuroinflammation when aged or challenged. Future studies should determine the precise physiological role of *Slco2b1*-mediated microglial heme uptake in disease and physiology.

Limitations of the Study

In this study, we conducted several gain-of-function screens using metabolism-scale CRISPRa libraries. While activation of gene expression by CRISPRa can identify genes with redundant functions in well-designed experiments followed by validation assays, it should be noted that overexpression could result in neomorphic phenotypes that may be physiologically irrelevant. Therefore, loss-of-function assays should be carried out to investigate relevance of the gene function in particular phenotypes. In addition, we hereby characterized heme as a substrate of SLCO2B1, while leaving open the possibility that it can be a broad-spectrum transporter with other physiological substrates. Indeed, steroid hormone conjugates, xenobiotics, and co-porphyrins were implicated as SLCO2B1 substrates in previous biochemical assays (Medwid et al., 2021). To precisely calculate the affinity of SLCO2B1 for heme and compare it to those of other transporters, liposome-based *in vitro* reconstituted uptake assays should be conducted in future work.

STAR METHODS

RESOURCE AVAILABILITY

Lead Contact—Further information and requests for resources and reagents should be directed to and will be fulfilled by the Lead Contact, Kıvanç Birsoy (kbirsoy@rockefeller.edu)

Materials Availability—All unique reagents generated in this study are available from the lead contact upon request.

Data and code availability

- Original western blot images have been deposited on Mendeley at https://doi.org/10.17632/sg3b3f25p4.1 and are publicly available as of the date of publication. The DOI is also listed in the key resources table.
- This paper does not report original code.
- Any additional information required to reanalyze the data reported in this paper is available from the lead contact upon request.

EXPERIMENTAL MODEL AND SUBJECT DETAILS

Mice—All animal studies were performed according to a protocol approved by the Institutional Animal Care and Use Committee (IACUC) at Rockefeller University. Animals were housed in ventilated caging on a standard light-dark cycle with food and water *ad libitum*. The mouse strain C57BL/6N-Slco2b1$^{tm1a(KOMP)Wtsi}$/Mmucd (MMRRC line: 049765-UCD) was recovered from cryopreserved sperm obtained from Mutant Mouse Resource and Research Center (MMRRC) at University of California, Davis. C57BL/6N-Slco2b1$^{tm1a(KOMP)Wtsi}$/Mmucd sperm was crossed to C57BL/6J wild-type strain (from The Jackson Laboratory) through *in vitro* fertilization at Rockefeller University Transgenic and Reproductive Technology Center. The progeny is maintained under standard conditions and identified through PCR amplification-based genotyping method provided by MMRRC. Homozygous mutant and homozygous wild type female animals of 5-8 weeks were used in microglia isolation experiments. Genotypes were revealed to blinded investigators post-analysis.

Cell Lines, Compounds and Constructs—Jurkat, HepG2, HEK293T and MDA-MB-231 cell lines were purchased from ATCC. Other cell lines were kindly provided by the following investigators: PaTu-8988t pancreatic adenocarcinoma cell line by Dr. Monther Abu-Remaileh (Stanford University, CA), the HY15549 mouse pancreatic cancer line by Nabeel El-Bardeesy (Massachusetts General Hospital Cancer Center, MA), AK196 mouse pancreatic cancer line by Haoqiang Yang (MD Anderson Cancer Center, TX), 4T1 and 4T07 mouse breast cancer cell lines by Dr. Sohail Tavazoie (Rockefeller University, NY). All cell lines were verified to be mycoplasma contamination-free and authenticated by STR profiling. Reagents, compounds, and antibodies used in this study are listed in Table S1.

Cell Culture Conditions—Unless otherwise indicated, all listed cell lines, except for HepG2, were cultured in RPMI-1640 media (GIBCO) containing 2mM glutamine, 10% fetal bovine serum (SAFC, Sigma Aldrich) and 1% penicillin and streptomycin (Invitrogen). HepG2 cells were cultured in DMEM (GIBCO) containing 4.5g/L glucose, 110mg/L pyruvate, 4mM glutamine, supplemented with 10% fetal bovine serum and 1% penicillin and streptomycin. All cells were maintained at 37°C, 21% O_2 and 5% CO_2. For Figure S3, Jurkat cells were cultured in RPMI1640 supplemented with dialyzed FBS (GIBCO #26400-044).

METHOD DETAILS

Generation of overexpression and knockout constructs—Gene fragments for coding sequences of human *SLCA25A37*, *SLCO2B1*, *SLCO2A1*; and mouse *Slco2b1* were purchased from Twist Biosciences, then cloned into pLV-EF1a-IRES-Blast vector (Addgene #85133) by Gibson assembly method. pLV-EF1a-IRES-Blast was used as a control vector control in overexpression experiments. Knockout cells were generated with CRISPR/Cas9 method. Forward and reverse oligos targeting *TFRC*, *UROD* and *HMOX2* were annealed and ligated into BsmBI-linearized pLentiCRISPR v2 vector.

Cell proliferation assays—2,000 Jurkat cells or 500 PaTu-8988t or 500 mouse KPC cells/ per well were seeded, in triplicates, in 0.2 mL RPMI-1640 medium containing indicated treatments in 96-well plates. On the day of seeding and the final day of treatment (as indicated in corresponding figures), 40 μL of CellTiter-Glo reagent (Promega) was added, then, luminescence was measured on a SpectraMax M3 plate reader (Molecular Devices). Data are presented as cell doublings or the log2 fold change in luminescence on final treatment day compared to initial reading on the day of seeding.

Generation of knockout and overexpression cell lines—For generation of knockout cells, VSV-G and Delta-VPR lentiviral packaging vectors were simultaneously transfected into HEK293T cells along with plentiCRISPR v2 vector expressing Cas9 and the gene-targeting sgRNA, using XtremeGene9 transfection reagent (Roche). Similarly, for overexpression, pLV-EF1a-IRES-Blast vector containing the gene-of-interest was transfected along with lentiviral packaging vectors VSV-G and Delta-VPR. 60 h post-transfection, the supernatant was collected after passing through a 0.45 μm syringe filter. For transduction, 1 x 10^5 cells were plated in 6-well plates containing 4 μg/mL polybrene and virus, and then spin-infected by centrifugation at 2,200 rpm for 80 minutes. Mixed population knockouts were selected with puromycin; overexpression cells were selected with blasticidin. Knockout and/or overexpression efficiency was assessed via immunoblotting. Jurkat or PaTu-8988t cells expressing dCas9-VPR were generated following a similar lentiviral transduction strategy. Instead, Edit-R Lentiviral CRISPRa dCas9-VPR vector (Horizon Discovery) was used as the overexpression vector. Single cell clones overexpressing dCas9-VPR were generated by FACS sorting single cells on a BD FACSAriaII, 72-96 h post-infection into 96 well plates and grown for 2 weeks. Clones with strong overexpression were identified by Cas9 immunoblotting.

CRISPR/Cas9 genetic screens—For metabolic scale CRISPRa screens in human cell lines, a metabolism-focused sgRNA library was designed and screens were performed following established protocols (Birsoy et al., 2015; Wang et al., 2015) with the following details and modifications. To specifically focus on metabolic pathways, 2,989 genes encoding for metabolic enzymes and small molecule transporters, as described in Birsoy et al., 2015, were targeted with a total of 32,460 CRISPRa sgRNAs, whose designing approach was described previously (Horlbeck et al., 2016), and 49 non-targeting sgRNAs were included as controls. Sequences of sgRNAs included in human metabolism-focused CRISPRa library are provided in Table S1. Oligonucleotides containing sgRNA sequences were synthesized by Agilent Technologies, PCR amplified and cloned into lentiGuide-Puro vector (Addgene #52963). Briefly, amplicons were inserted into BsmBI-linearized lentiGuide-Puro vector by Gibson Assembly (NEB). Then, Gibson Assembly products were transformed into *E. coli* 10G SUPREME electrocompetent cells (Lucigen). This plasmid pool was used to produce lentivirus-containing supernatants in HEK293T cells. The titer of lentiviral supernatants was determined by infecting target cells at several amounts of virus in the presence of polybrene (4 μg/mL), counting the number of puromycin-resistant infected cells 3 days post-selection. For CRISPRa positive selection screens, 4 million target cells were infected at an MOI of ~0.7 and selected with puromycin (4 μg/mL) 72 h post-infection. An initial pool of 4 million cells was harvested for genomic DNA extraction. The remaining cells were cultured for 14 doublings under specified drug treatment or untreated control conditions. On the final day of screening, cells were harvested for genomic DNA extraction. sgRNA inserts were PCR amplified, purified, and sequenced on MiSeq platform (Illumina). Sequencing reads were aligned to the library of sgRNA sequences and the abundance of each sgRNA was tallied. Results were reported as percentage of total sgRNA reads acquired per gene, gene score or differential gene score. Percent total sgRNA reads was calculated by summing up all sgRNA reads mapped to a gene and calculating the percentage of this sum to the number of sgRNA reads acquired from the entire population. sgRNA scores, representing the log2 fold change of the normalized final read count of the sgRNA from the initial read count of the sgRNA, were calculated. Gene score is defined as the median $\log_2$ fold change of all sgRNAs targeting the gene in the abundance of all sgRNAs targeting that gene, between the initial and final population. The differential gene score refers to the difference between the gene scores of drug-treated and untreated control groups.

For metabolic scale CRISPRa screens in mouse AK196 pancreas cell line, a metabolism-focused sgRNA library was designed and screens were performed similarly, as described above. For these screens, 1,839 metabolic genes were targeted with a total of 17,031 CRISPRa sgRNAs. Sequences of sgRNAs included in mouse metabolism-focused CRISPRa library are provided in Table S2.

Metabolism-focused CRISPR knockout screens in human lines were performed following the screen protocol detailed above with the following modifications. 3×10^7 cells were infected with sgRNA library containing 23,971 sgRNAs targeting metabolic genes as reported by Zhu et al. (Zhu et al., 2019). Abundance of sgRNAs was quantified post-sequencing on NextSeq500 platform (Illumina). Full results of all CRISPR screens can be found in Supplemental Tables S4-S18.

Metabolite Profiling—For bulk metabolite profiling, 1 x10^6 Jurkat cells, in triplicate, were grown for 24 h under DFO-, BafA1-treatment or untreated conditions. Then, cells were rinsed in 0.9 % NaCl twice. Polar metabolites were extracted in 80 % methanol containing ^{15}N and ^{13}C fully-labeled amino acid standards (MSK-A2-1.2, Cambridge Isotope Laboratories, Inc). Extracts were shaken for 10 min with a vortexer, spun at 19,000 g to remove insoluble cell debris, nitrogen-dried and stored at −80°C until liquid chromatography-mass spectrometry analysis (LC-MS). Then, LC-MS analysis was conducted on a QExactive benchtop orbitrap mass spectrometer equipped with an Ion Max source and a HESI II probe coupled to a Dionex UltiMate 3000 UPLC system (Thermo Fisher Scientific). External mass calibration was performed using the standard calibration mixture every 7 days. Air dried polar samples were resuspended in 100 µL water and 2 µL were injected into a ZIC-pHILIC 150 × 2.1 mm (5 µm particle size) column (EMD Millipore). Chromatographic separation was achieved using the following conditions: Buffer A was 20 mM ammonium carbonate, 0.1% ammonium hydroxide; buffer B was acetonitrile. The column oven and autosampler tray were held at 25°C and 4°C, respectively. The chromatographic gradient was run at a flow rate of 0.150 mL/min as follows: 0–20 min: linear gradient from 80% to 20% B; 20–20.5 min: linear gradient from 20% to 80% B; 20.5–28 min: hold at 80% B. The mass spectrometer was operated in fullscan, polarity switching mode with the spray voltage set to 3.0 kV, the heated capillary held at 275°C, and the HESI probe held at 350°C. The sheath gas flow was set to 40 units, the auxiliary gas flow was set to 15 units, and the sweep gas flow was set to 1 unit. The MS data acquisition was performed in a range of 70–1000 m/z, with the resolution set at 70,000, the AGC target at 10^6, and the maximum injection time at 20 msec. Relative metabolite abundances were quantified using XCalibur QualBrowser 2.2 and Skyline Targeted Mass Spec Environment (MacCoss Lab) using a 5 ppm mass tolerance and a pooled-library of metabolite standards to verify metabolite identity. Relative metabolite levels were calculated by normalizing to total protein levels, as measured by Bicinchoninic Acid Assay (BCA).

Measurement of Metals by Inductively Couple Plasma / Mass Spectrometry (ICP/MS)—3 x10^7 Jurkat cells were seeded in triplicates and grown in standard culture conditions for 24 h. Cell pellets were collected and stored at −80°C until ICP/MS analysis. The cell pellet was resuspended in pure, distilled water of ≥80 µl. The cell pellet was lysed on ice, using 5 pulses with a cell disruptor/sonicator microtip. For each ICP/MS replicate, 30 to 50 µl of cell lysate was digested using a 5:1 mixture of nitric acid (OPTIMA grade, 70%, Fisher Scientific) and ultrapure hydrogen peroxide (ULTREX II, 30%, Fisher Scientific). 30 lysate, 500 uL of nitric acid and 100 uL hydrogen peroxide are added to 2 mL polypropylene tubes. This mixture was allowed to digest overnight at room temperature, heated at 95°C just until dry, and resuspended overnight in 1 ml of 2% nitric acid for analysis. The mixture was mixed well the following day to ensure resuspension, and 800 µl more 2% nitric acid is added along with 200 µl of 10X internal standard (prepared in 2% nitric acid). For ICP/MS run, an Agilent 7900 ICP/MS instrument was operated in helium (He) collision cell gas mode for all measurements. Elements were measured at the following isotopes: 56Fe, 55Mn, 63Cu, 66Zn. Calibration standards and samples were prepared in an acid matrix of 2% OPTIMA Grade Nitric Acid. Solutions of Agilent Multi-element Calibration Standard 2A were prepared to obtain an eight-point calibration curve. Agilent Germanium (or Scandium)

Standard(s) were added to calibration standards, blanks, and samples. Standards were used to correct for potential sample matrix and/or nebulization effects.

Amounts of metals within a sample were normalized by total amount of protein, as determined by BCA assay (Thermo Fisher Scientific).

Immunoblotting—1 x 10^6 cells were washed in cold PBS and lysed in a buffer containing 10 mM Tris-HCl pH 7.4, 150 NaCl, 1 mM EDTA, 1% Triton X-100, 2% SDS, 0.1% CHAPS, and protease inhibitors (Milipore Sigma). Lysates were sonicated, centrifuged at 1,000 g, and supernatant was collcted as the protein lysate. Total protein quantified using BCA Protein Assay Kit (Thermo Fisher) with bovine serum albumin as a protein standard. Protein samples were resolved on 8% or 10%–20% SDS-PAGE gels (Novex, ThermoFisher) and analyzed by standard immunoblotting protocol. Briefly, PVDF membranes (Milipore) were incubated with primary antibodies at 4°C overnight. After washing off the primary antibodies in tris buffered saline/ 0.1% Tween-20 (TBS-T), secondary antibody incubation was performed at room temperature for 1h. Secondary antibodies including anti-mouse IgG–HRP linked (Cell Signaling, 7076) and anti-rabbit IgG–HRP linked (Cell Signaling, 7074), were used at 1:3,000 dilution. Blots were developed by ECL Chemiluminescent detection system (Perkin Elmer LLC) and film exposure. SRX-101A Film Processor (Konica Minolta) and Premium autoradiography Films (Thomas Scientific) were used for developing.

Immunocytochemistry and Confocal Microscopy—PaTu-8988t cells were seeded on coverslips and grown overnight at 37°C with 5% CO_2. Next day, cells were fixed in 4 % PFA at room temperature for 15 min, permeabilized in 1% triton X-100 in PBA, and then, blocked in 1% bovine serum albumin (Sigma) for 30 min at room temperature. Primary antibody incubation was performed overnight at 4°C. Then, cells were rinsed in PBS twice and secondary antibody incubation was performed at room temperature for 30 min. After washing twice in PBS, DAPI, nuclear counterstain, incubation was performed at room temperature for 10 min, then cells were washed twice in PBS and mounted in ProLong Gold antifade mountant (Molecular Probes). Slides were imaged with Nikon A1R MP multiphoton microscope with confocal modality, using Nikon Plan Apo γ 60X/1.40 oil immersion objective.

Real-time quantitative PCR—Total RNA was isolated from mouse livers using TRIzol reagent (Thermo Fisher Scientific), following manufacturer's manual. After DNase I treatment (New England Biolabs), 1 μg total RNA was used for cDNA synthesis with Superscript III RT kit (Invitrogen). qPCR was performed on a Thermo QuantStudio 6 Flex Real-Time PCR machine. The primer sequences were listed in Table S19. Gene expression levels were normalized to beta-actin using ΔΔCt method.

Zinc Mesoporphyrin (ZnMP) Uptake and Flow Cytometry Analysis—Adherent cells (HepG2, PaTu-8988t and KP pancreas) were trypsinized and washed with 1X Hank's Balanced Salt Solution (HBSS) (Milipore Sigma) twice. 1 x10^5 cells were placed in a microfuge tube and incubated with the indicated concentration of ZnMP (Frontier Scientific) in 1x HBSS for 15 min at room temperature. Uptake was terminated by placing cells on ice. Then, cell pellets were collected, washed twice in 1X HBSS and resuspended in cold

FACS buffer (DPBS + 2% FBS + 5mM EDTA). ZnMP uptake was assessed by Flow Cytometry (Attune NxT Flow Cytometer, Thermo Fisher). 10,000 events were recorded per each sample. ZnMP signal was detected by exciting with 561 nm laser, AlexaFluor 568 emission track was recorded as it overlaps with ZnMP emission. Data were analyzed and plotted with FCS Express 7 Research software, version 7.12 (De Novo Software, Inc).

For ZnMP uptake in Jurkat cells, 5μM ZnMP was diluted directly in culture media (RPMI 1640 + 10% FBS). Cells were treated with ZnMP overnight at standard culture conditions (37°C, 5% CO_2). After that, Jurkat cells were washed twice in PBS and resuspended in FACS buffer. Flow cytometry and data analyses were carried out as described above.

For dose and time-dependent ZnMP uptake assays, mouse KP pancreas cells were used. Cells, in triplicate, were treated with 1:2 serial dilutions of ZnMP, between 0.125 μM and 1μM, including 0 μM control (equal volume DMSO), for 15 minutes at room temperature. For time course uptake assay, cells, in triplicate, were treated with 1 μM ZnMP for 0, 1, 2, 5 and 10 minutes at room temperature. Median fluorescence value of $ZnMP^+$-gated population and number of gated events were multiplied to calculate total ZnMP fluorescence. Results were plotted in Prism 9 (GraphPad) as dose or time vs. total ZnMP fluorescence.

Mouse microglia isolation and ZnMP uptake assay—Mouse microglial cells were isolated from 8-10 week-old female mice as previously described (Ledo et al., 2020). Briefly, mice were sacrificed, whole brains were removed and placed in DPBS (Ca^{2+} and Mg^{2+} free) containing 5% FBS and 1mM HEPES pH7.4. Brain tissue was minced with scissors and incubated in 4,000 U/ml of collagenase D (Roche) at 37°C for 30 minutes. Collagenase digestion was stopped by adding 10 mM EDTA and incubating for additional 5 minutes at 37°C. Digested tissue was passed through 70-μm cell strainer, centrifuged at 2,000 rpm, washed in DPBS, and centrifuged in 38% Percoll gradient for 30 min. Cell pellet containing microglia fraction was washed and resuspended in cold FACS buffer (DPBS + 2% FBS + 5mM EDTA). Non-specific binding was blocked by incubation with Fc blocking antibody (BD Biosciences, Clone 2.4G2) for 15 min. Cells were washed in FACS buffer and stained with Cx3cr1 antibody (Clone: SA011F11) conjugated to PE/Cy7. After that, cells were washed twice in FACS buffer to remove unbound, excess antibody. 5 $x10^5$ cells were placed in a microfuge tube and incubated with 2 μM ZnMP (Frontier Scientific) in 1x HBSS for 15 min at room temperature. Uptake was terminated by placing the cells on ice. Then, cell pellets were collected, washed twice in 1X HBSS and resuspended in cold FACS buffer (DPBS + 2% FBS + 5mM EDTA). ZnMP uptake was assessed by Flow Cytometry (Attune NxT Flow Cytometer, Thermo Fisher). 10,000 events were recorded per each sample. ZnMP signal was detected by exciting with 561 nm laser, AlexaFluor 568 emission track was recorded. Cx3cr1-PE/Cy7 signal was detected by exciting with 488 nm laser and recording emission at 780 nm. Data were analyzed and plotted with FCS Express 7 Research software, version 7.12 (De Novo Software, Inc).

Sorting microglial cells with FACS and RNA-seq—Mouse microglial cells were isolated as described above. For FACS, cells were stained with Cx3cr1-PE/Cy7 (clone:SA011F11) , CD11b-Brilliant Violent 711 (clone: M1/70) and Ly6C-Brilliant Violet 510 (clone: HK1.4) and DAPI for viability. Next, Cx3cr1+ CD11b+ Ly6C− DAPI−

population was sorted directly into TRIzol-LS with BD FACS Aria II. Then, total RNA was isolated following TRIzol-LS (Thermo Fisher Scientific) manufacturer's manual. RNA concentrations were determined using Qubit 2.0 Fluorometer (Life Technologies); RNA intregrity was checked using Agilent TapeStation 4200 (Agilent Technologies). RNA sequencing library was prepared using NEBNext Ultra RNA library kit for Illumina (NEB) following manufacturer's manual. The sequencing libraries were clustered on a single lane of a flowcell. Afterwards, the flowcell was loaded on the Illumina HiSeq instrument (4000 or equivalent) according to manufacturer's guidelines. The samples were sequenced using a 2x150bp Paired End (PE) configuration. For RNA-seq analysis, sequence and transcript coordinates for mouse genome (mm 10 UCSC) and gene models were retrieved from the Bioconductor Bsgenome.Hsapiens.UCSC.mm10 (version 1.4.0) and TxDb.Hsapiens.UCSC.mm10.knownGene (version 3.4.0) Bioconductor libraries respectively. Transcript expressions were calculated using the Salmon quantification software (Patro et al., 2017) (version 0.8.2) and gene expression levels as transcripts per million (TPM). Normalization and rlog transformation of raw read counts in genes were performed using DESeq2 (Love et al., 2014) (version 1.20.0). Genes significantly differentially expressed between conditions were identified using DESeq2 with a Benjamini Hochberg adjusted p-value cutoff of 0.05. Gene Ontology term enrichment was obtained for all genes significantly differentially expressed between conditions (absolute logFC > 0, adjusted p-value < 0.05) using the fisher test in the topGO Bioconductor package and ranked using the elim algorithm and functional annotation from the org.Mm.eg.db Bioconductor package (version 3.10).

Quantification and statistical analysis

Statistical analysis was performed with built-in statistics tools in Prism9 (GraphPad Software). Statistical tests, error bars and confidence intervals can be found in the figure legends. p-values for comparisons between groups are indicated in figures.

Supplementary Material

Refer to Web version on PubMed Central for supplementary material.

ACKNOWLEDGEMENTS

We thank all members of the Birsoy laboratory for helpful suggestions. G.U. is a Damon Runyon Fellow, supported by the Damon Runyon Cancer Research Foundation (DRG-2431-21), and by the grant UL1 TR001866 from the National Center for Advancing Translational Sciences (NCATS, National Institutes of Health (NIH) Clinical and Translational Science Award (CTSA) program. H.-W.Y is supported by a *C. H. Li Memorial Scholar Fund Award* at The Rockefeller University. K.B. is supported by the NIH/NCI (DP2 OD024174-01), NIH/NIDDK (R01 DK123323-01), Pershing Square Sohn Foundation and Mark Foundation Emerging Leader Award; and is a Searle and Pew-Stewart Scholar.

REFERENCES

Andreini C, Putignano V, Rosato A, and Banci L (2018). The human iron-proteome. Metallomics : integrated biometal science 10. 10.1039/c8mt00146d.

Aregger M, Lawson KA, Billmann M, Costanzo M, Tong AHY, Chan K, Rahman M, Brown KR, Ross C, Usaj M, et al. (2020). Systematic mapping of genetic interactions for de novo fatty acid

synthesis identifies C12orf49 as a regulator of lipid metabolism. Nature metabolism 2. 10.1038/s42255-020-0211-z.

Birsoy K, Wang T, Chen W, Freinkman E, Abu-Remaileh M, and Sabatini DM (2015). An essential role of the mitochondrial electron transport chain in cell proliferation is to enable aspartate synthesis. Cell 162, 540–551. 10.1016/j.cell.2015.07.016. [PubMed: 26232224]

Bollinger JM Jr, Edmondson DE, Huynh BH, Filley J, Norton JR, and Stubbe J (1991). Mechanism of assembly of the tyrosyl radical-dinuclear iron cluster cofactor of ribonucleotide reductase. Science (New York, N.Y.) 253. 10.1126/science.1650033.

Cao J, O'Day DR, Pliner HA, Kingsley PD, Deng M, Daza RM, Zager MA, Aldinger KA, Blecher-Gonen R, Zhang F, et al. (2020). A human cell atlas of fetal gene expression. Science (New York, N.Y.) 370. 10.1126/science.aba7721.

Chambers IG, Willoughby MM, Hamza I, and Reddi AR (2021). One ring to bring them all and in the darkness bind them: The trafficking of heme without deliverers. Biochimica et biophysica acta. Molecular cell research 1868. 10.1016/j.bbamcr.2020.118881.

Cho HP, Nakamura M, and Clarke SD (1999). Cloning, expression, and fatty acid regulation of the human delta-5 desaturase. The Journal of biological chemistry 274. 10.1074/jbc.274.52.37335.

Devkota R, Svensk E, Ruiz M, Ståhlman M, Borén J, and Pilon M (2017). The adiponectin receptor AdipoR2 and its Caenorhabditis elegans homolog PAQR-2 prevent membrane rigidification by exogenous saturated fatty acids. PLoS Genetics 13. 10.1371/journal.pgen.1007004.

Duffy SP, Shing J, Saraon P, Berger LC, Eiden MV, Wilde A, and Tailor CS (2010). The Fowler syndrome-associated protein FLVCR2 is an importer of heme. Molecular and cellular biology 30. 10.1128/MCB.00690-10.

Fernández-Mendívil C, Luengo E, Trigo-Alonso P, García-Magro N, Negredo P, and López MG (2021). Protective role of microglial HO-1 blockade in aging: Implication of iron metabolism. Redox biology 38. 10.1016/j.redox.2020.101789.

Garcia-Bermudez J, Baudrier L, La K, Zhu XG, Fidelin J, Sviderskiy VO, Papagiannakopoulos T, Molina H, Snuderl M, Lewis CA, et al. (2018). Aspartate is a limiting metabolite for cancer cell proliferation under hypoxia and in tumours. Nat Cell Biol 20, 775–781. 10.1038/s41556-018-0118-z. [PubMed: 29941933]

Goldstein JL, and Brown MS (2009). The LDL receptor. Arteriosclerosis, thrombosis, and vascular biology 29. 10.1161/ATVBAHA.108.179564.

Grube M, Köck K, Karner S, Reuther S, Ritter CA, Jedlitschky G, and Kroemer HK (2006). Modification of OATP2B1-mediated transport by steroid hormones. Molecular pharmacology 70. 10.1124/mol.106.026450.

Horlbeck MA, Gilbert LA, Villalta JE, Adamson B, Pak RA, Chen Y, Fields AP, Park CY, Corn JE, Kampmann M, and Weissman JS (2016). Compact and highly active next-generation libraries for CRISPR-mediated gene repression and activation. eLife 5. 10.7554/eLife.19760.

Jiang Y, Li C, Wu Q, An P, Huang L, Wang J, Chen C, Chen X, Zhang F, Ma L, et al. (2019). Iron-dependent histone 3 lysine 9 demethylation controls B cell proliferation and humoral immune responses. Nature communications 10. 10.1038/s41467-019-11002-5.

Kaplan J, and Ward DM (2013). The essential nature of iron usage and regulation. Current Biology 23. 10.1016/j.cub.2013.05.033.

Kenkhuis B, Somarakis A, de Haan L, Dzyubachyk O, IJsselsteijn ME, de Miranda NFCC, Lelieveldt BPF, Dijkstra J, van Roon-Mom WMC, Höllt T, and van der Weerd L (2021). Iron loading is a prominent feature of activated microglia in Alzheimer's disease patients. Acta Neuropathologica Communications 9. 10.1186/s40478-021-01126-5.

Klempner MS, and Styrt B (1983). Alkalinizing the intralysosomal pH inhibits degranulation of human neutrophils. The Journal of clinical investigation 72. 10.1172/JCI111139.

Krasemann S, Madore C, Cialic R, Baufeld C, Calcagno N, El Fatimy R, Beckers L, O'Loughlin E, Xu Y, Fanek Z, et al. (2017). The TREM2-APOE Pathway Drives the Transcriptional Phenotype of Dysfunctional Microglia in Neurodegenerative Diseases. Immunity 47. 10.1016/j.immuni.2017.08.008.

König J (2011). Uptake transporters of the human OATP family: molecular characteristics, substrates, their role in drug-drug interactions, and functional consequences of polymorphisms. In Handbook of Experiemental Pharmacology, (Handb Exp Pharmacol). 10.1007/978-3-642-14541-4_1.

Lanfranco MF, Sepulveda J, Kopetsky G, and Rebeck GW (2021). Expression and secretion of apoE isoforms in astrocytes and microglia during inflammation. Glia 69. 10.1002/glia.23974.

Ledo JH, Zhang R, Mesin L, Mourão-Sá D, Azevedo EP, Troyanskaya OG, Bustos V, and Greengard P (2020). Lack of a site-specific phosphorylation of Presenilin 1 disrupts microglial gene networks and progenitors during development. PloS one 15. 10.1371/journal.pone.0237773.

Leitner DF, and Connor JR (2012). Functional roles of transferrin in the brain. Biochimica et Biophysica Acta 1820. 10.1016/j.bbagen.2011.10.016.

Levade T, Leruth M, Graber D, Moisand A, Vermeersch S, Salvayre R, and Courtoy PJ (1996). In situ assay of acid sphingomyelinase and ceramidase based on LDL-mediated lysosomal targeting of ceramide-labeled sphingomyelin. Journal of lipid research 37.

Love MI, Huber W, and Anders S (2014). Moderated estimation of fold change and dispersion for RNA-seq data with DESeq2. Genome Biol 15, 550. 10.1186/s13059-014-0550-8. [PubMed: 25516281]

Medwid S, Li MMJ, Knauer MJ, Lin K, Mansell SE, Schmerk CL, Zhu C, Griffin KE, Yousif MD, Dresser GK, et al. (2019). Fexofenadine and Rosuvastatin Pharmacokinetics in Mice with Targeted Disruption of Organic Anion Transporting Polypeptide 2B1. Drug metabolism and disposition: the biological fate of chemicals 47. 10.1124/dmd.119.087619.

Medwid S, Price HR, Taylor DP, Mailloux J, Schwarz UI, Kim RB, and Tirona RG (2021). Organic Anion Transporting Polypeptide 2B1 (OATP2B1) Genetic Variants: In Vitro Functional Characterization and Association With Circulating Concentrations of Endogenous Substrates. Frontiers in pharmacology 12. 10.3389/fphar.2021.713567.

Meister A (1995). Mitochondrial changes associated with glutathione deficiency. Biochimica et biophysica acta 1271. 10.1016/0925-4439(95)00007-q.

Moos T, and Morgan EH (1998). Evidence for low molecular weight, non-transferrin-bound iron in rat brain and cerebrospinal fluid. Journal of Neuroscience Research 54. 10.1002/(SICI)1097-4547(19981115)54:4<486::AID-JNR6>3.0.CO;2-I.

Mracsko E, and Veltkamp R (2014). Neuroinflammation after intracerebral hemorrhage. Frontiers in cellular neuroscience 8. 10.3389/fncel.2014.00388.

Patro R, Duggal G, Love MI, Irizarry RA, and Kingsford C (2017). Salmon provides fast and bias-aware quantification of transcript expression. Nature Methods 14. 10.1038/nmeth.4197.

Pavlova NN, Hui S, Ghergurovich JM, Fan J, Intlekofer AM, White RM, Rabinowitz JD, Thompson CB, and Zhang J (2018). As Extracellular Glutamine Levels Decline, Asparagine Becomes an Essential Amino Acid. Cell metabolism 27. 10.1016/j.cmet.2017.12.006.

Pisoni RL, Acker TL, Lisowski KM, Lemons RM, and Thoene JG (1990). A cysteine-specific lysosomal transport system provides a major route for the delivery of thiol to human fibroblast lysosomes: possible role in supporting lysosomal proteolysis. The Journal of Cell Biology 110. 10.1083/jcb.110.2.327.

Possemato R, Marks KM, Shaul YD, Pacold ME, Kim D, Birsoy K, Sethumadhavan S, Woo HK, Jang HG, Jha AK, et al. (2011). Functional genomics reveal that the serine synthesis pathway is essential in breast cancer. Nature 476. 10.1038/nature10350.

Rajagopal A, Rao AU, Amigo J, Tian M, Upadhyay SK, Hall C, Uhm S, Mathew MK, Fleming MD, Paw BH, et al. (2008). Haem homeostasis is regulated by the conserved and concerted functions of HRG-1 proteins. Nature 453. 10.1038/nature06934.

Richardson DR, and Ponka P (1997). The molecular mechanisms of the metabolism and transport of iron in normal and neoplastic cells. Biochimica et biophysica acta 1331. 10.1016/s0304-4157(96)00014-7.

Ruiz M, Ståhlman M, Borén J, and Pilon M (2019). AdipoR1 and AdipoR2 maintain membrane fluidity in most human cell types and independently of adiponectin. Journal of lipid research 60. 10.1194/jlr.M092494.

Ryle MJ, and Hausinger RP (2002). Non-heme iron oxygenases. Current opinion in chemical biology 6. 10.1016/s1367-5931(02)00302-2.

Sato T, Shapiro JS, Chang HC, Miller RA, and Ardehali H (2022). Aging is associated with increased brain iron through cortex-derived hepcidin expression. eLife 11. 10.7554/eLife.73456.

Shaw GC, Cope JJ, Li L, Corson K, Hersey C, Ackermann GE, Gwynn B, Lambert AJ, Wingert RA, Traver D, et al. (2006). Mitoferrin is essential for erythroid iron assimilation. Nature 440. 10.1038/nature04512.

Shen J, Wu G, Tsai AL, and Zhou M (2020). Structure and Mechanism of a Unique Diiron Center in Mammalian Stearoyl-CoA Desaturase. Journal of molecular biology 432. 10.1016/j.jmb.2020.05.017.

Sviderskiy VO, Terzi EM, and Possemato R (2019). Iron–Sulfur Cluster Metabolism Impacts Iron Homeostasis, Ferroptosis Sensitivity, and Human Disease. In Ferroptosis in Health and Disease., (Springer, Cham). 10.1007/978-3-030-26780-3_12.

Tabula Muris Consortium (2018). Single-cell transcriptomics of 20 mouse organs creates a Tabula Muris. Nature 562. 10.1038/s41586-018-0590-4.

Tsherniak A, Vazquez F, Montgomery PG, Weir BA, Kryukov G, Cowley GS, Gill S, Harrington WF, Pantel S, Krill-Burger JM, et al. (2017). Defining a Cancer Dependency Map. Cell 170. 10.1016/j.cell.2017.06.010.

Vargas JD, Herpers B, McKie AT, Gledhill S, McDonnell J, van den Heuvel M, Davies KE, and Ponting CP (2003). Stromal cell-derived receptor 2 and cytochrome b561 are functional ferric reductases. Biochimica et biophysica acta 1651. 10.1016/s1570-9639(03)00242-5.

Vasconcellos LRC, Martimiano L, Dantas DP, Fonseca FM, Mata-Santos H, Travassos L, Mendez-Otero R, Bozza MT, and Pimentel-Coelho PM (2021). Intracerebral Injection of Heme Induces Lipid Peroxidation, Neuroinflammation, and Sensorimotor Deficits. Stroke 52. 10.1161/STROKEAHA.120.031911.

Wang H, An P, Xie E, Wu Q, Fang X, Gao H, Zhang Z, Li Y, Wang X, Zhang J, et al. (2017). Characterization of ferroptosis in murine models of hemochromatosis. Hepatology (Baltimore, Md.) 66. 10.1002/hep.29117.

Wang T, Birsoy K, Hughes NW, Krupczak KM, Post Y, Wei JJ, Lander ES, and Sabatini DM (2015). Identification and characterization of essential genes in the human genome. Science 350. 10.1126/science.aac7041.

Wang Z, Guo R, Trudeau SJ, Wolinsky E, Ast T, Liang JH, Jiang C, Ma Y, Teng M, Mootha VK, and Gewurz BE (2021). CYB561A3 is the key lysosomal iron reductase required for Burkitt B-cell growth and survival. Blood 138. 10.1182/blood.2021011079.

Weber RA, Yen FS, Nicholson SPV, Alwaseem H, Bayraktar EC, Alam M, Timson RC, La K, Abu-Remaileh M, Molina H, and Birsoy K (2020). Maintaining Iron Homeostasis Is the Key Role of Lysosomal Acidity for Cell Proliferation. Mol Cell. 10.1016/j.molcel.2020.01.003.

White C, Yuan X, Schmidt PJ, Bresciani E, Samuel TK, Campagna D, Hall C, Bishop K, Calicchio ML, Lapierre A, et al. (2013). HRG1 is essential for heme transport from the phagolysosome of macrophages during erythrophagocytosis. Cell metabolism 17. 10.1016/j.cmet.2013.01.005.

Yager JY, and Hartfield DS (2002). Neurologic manifestations of iron deficiency in childhood. Pediatric neurology 27. 10.1016/s0887-8994(02)00417-4.

Zhu XG, Nicholson Puthenveedu S, Shen Y, La K, Ozlu C, Wang T, Klompstra D, Gultekin Y, Chi J, Fidelin J, et al. (2019). CHP1 Regulates Compartmentalized Glycerolipid Synthesis by Activating GPAT4. Mol Cell 74, 45–58.e47. 10.1016/j.molcel.2019.01.037. [PubMed: 30846317]

Highlights

- CRISPRa screens identify metabolic limitations for growth under stress conditions
- Expression of *SLCO2B1* confers resistance to iron limitation
- SLCO2B1-mediated heme uptake increases iron availability via heme oxygenase
- *SLCO2B1* is required for heme analog import in primary microglia

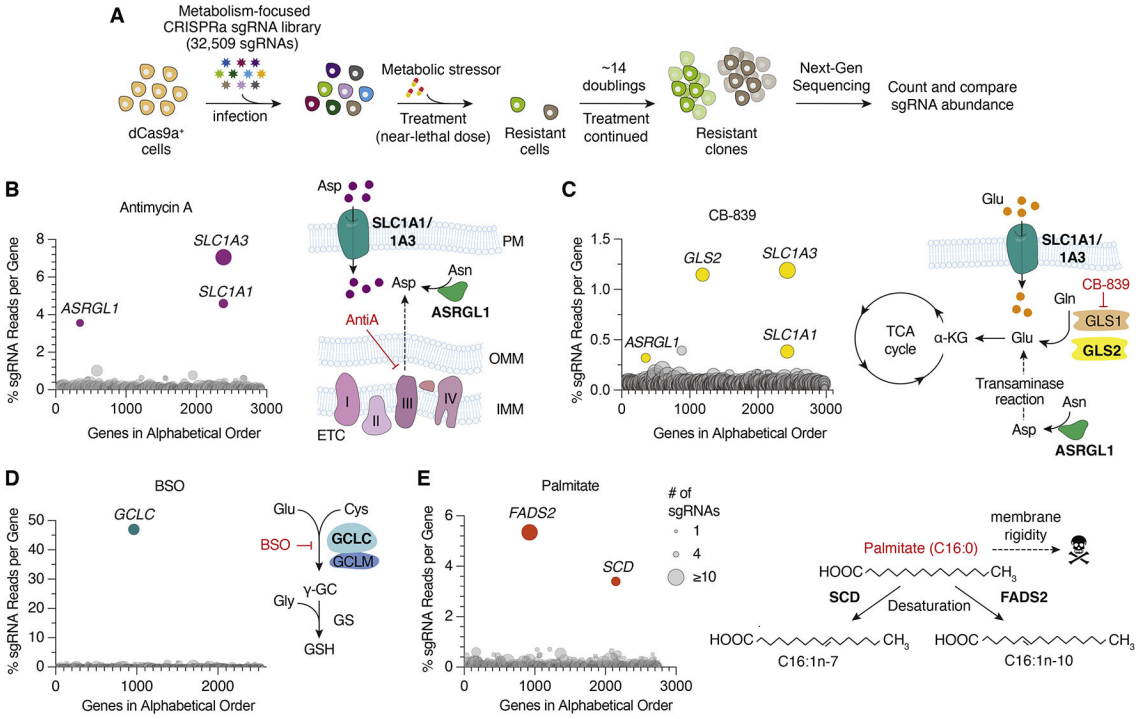

Figure 1. Metabolic-scale gene activation screens identify metabolic processes limiting for cell proliferation under stress conditions

(A) Scheme describing metabolism-focused positive selection CRISPRa screens.

(B-E) CRISPRa screen results for (B) Antimycin A (10 nM), (C) CB-839 (6 μM), (D) BSO (2 mM) in Pa-Tu 8988t dCas9a cells and (E) Palmitate (200 μM) in Jurkat dCas9a cells. Data were plotted as genes in alphabetical order vs. percentage of sgRNAs reads per gene. Percent total sgRNA reads was calculated by summing up all sgRNA reads mapped to a gene and calculating the percentage of this sum to the number of sgRNA reads acquired from the entire population. Bubble size indicates number of detected sgRNAs post-screen. See also Figure S1, Tables S1-S8

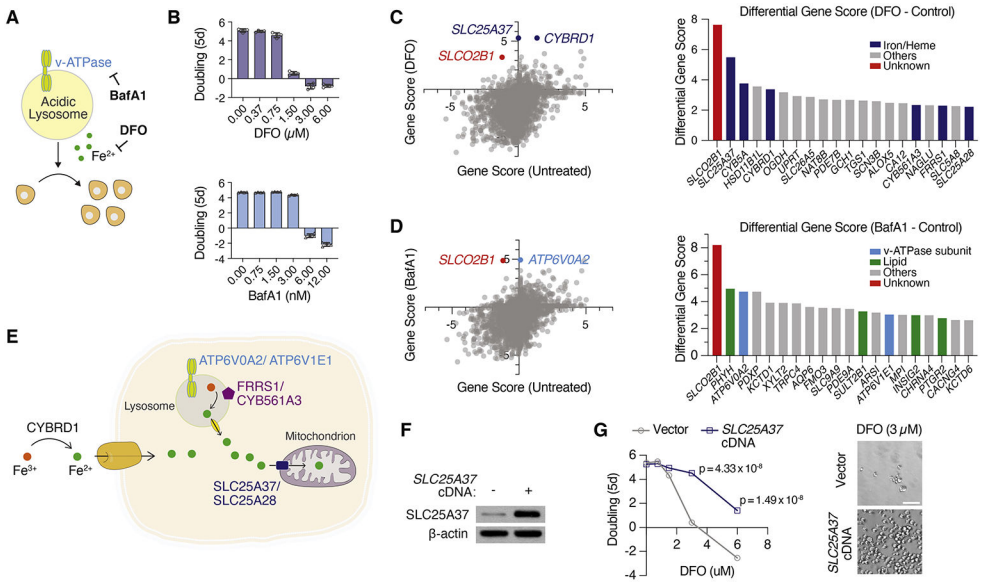

Figure 2. CRISPRa screens reveal metabolic genes conferring resistance to iron depletion

(A) BafA1 and DFO decreases cellular iron availability through different mechanisms.

(B) Dose-dependent effects of DFO and BafA1 on proliferation of Jurkat cells (Mean ± SEM, n = 5).

(C) Gene scores of untreated vs. DFO (2 μM)-treated Jurkat-dCas9a cells (left). Gene score is the median $\log_2$ fold change in the abundance of all sgRNAs targeting that gene during the screening period. Differential gene scores of top 20 genes providing resistance to DFO (right). Iron/heme-related genes are indicated in dark blue.

(D) Gene scores of untreated vs. BafA1 (5 nM)-treated Jurkat-dCas9a cells (left). Differential gene scores of top 20 genes providing resistance to BafA1 (right). Vacuolar ATPase subunits are indicated in light blue, lipid metabolism-related genes in green, other genes in gray.

(E) Scheme displaying selected scoring genes conferring resistance to iron-restriction.

(F) Immunoblot analysis of control and *SLC25A37*-overexpressing Jurkat cells. β-actin was used as loading control.

(G) Fold change in the number ($\log_2$) of control vector and *SLC25A37*-overexpressing cells after 5 days in the presence of indicated DFO concentrations (left). Representative bright-field micrographs of Jurkat cells after 5-day treatment with 3 μM DFO (right). Scale bar is 50 μM.

See also Figures S1-S3, Tables S9-S14

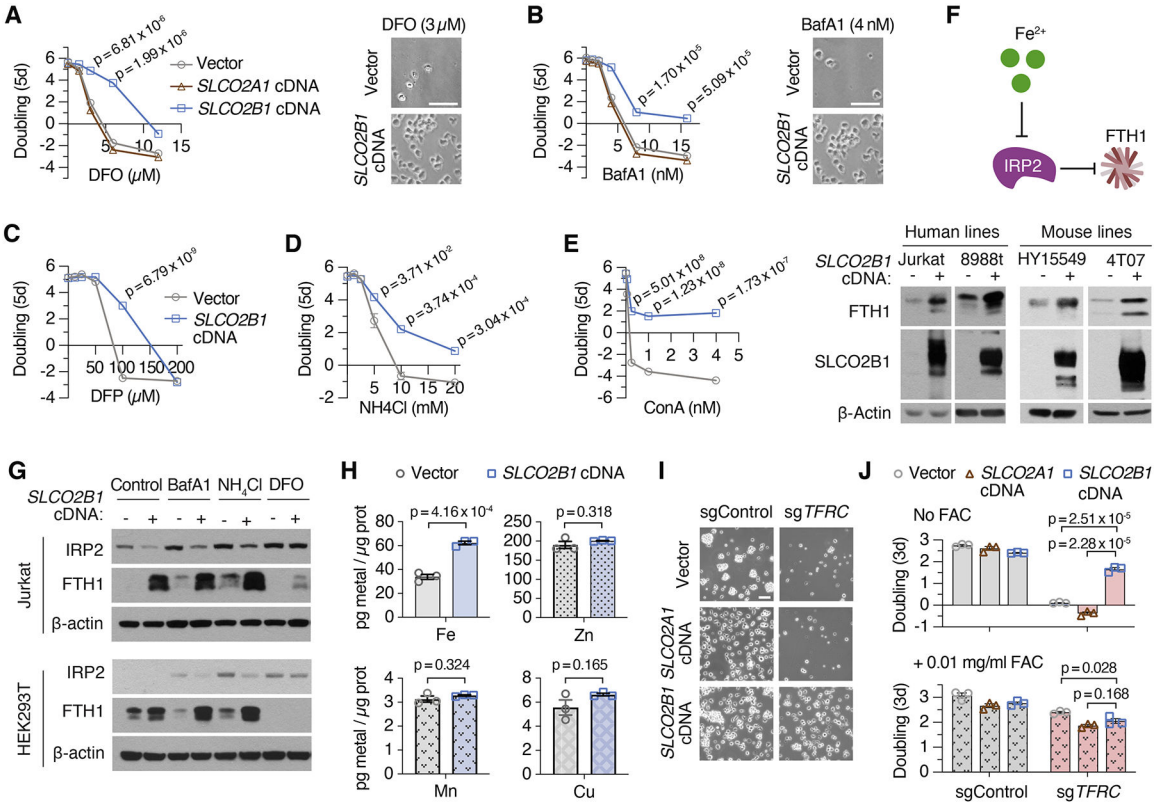

Figure 3. *SLCO2B1* expression is sufficient to promote iron availability and sustain cell proliferation under iron restriction

(A) Fold change in the number (log_2) of vector, *SLCO2A1* and *SLCO2B1*-expressing cells after 5 days in the presence of indicated DFO concentrations (left). Representative bright-field micrographs of Jurkat cells after 5-day treatment with 3 μM DFO (right). Scale bar is 50 μm.

(B) Fold change in the number (log_2) of vector, *SLCO2A1* and *SLCO2B1*-expressing cells after 5 days in the presence of indicated BafA1 concentrations (left) and representative bright-field micrographs of Jurkat cells after 5-day treatment with 4 nM BafA1 (right). Scale bar is 50 μm.

(C-E) Fold change in the number (log_2) of vector and *SLCO2B1*-expressing cells after 5 days in the presence of indicated (C) DFP, (D) NH_4Cl and (E) ConA concentrations

(F) Schematic (top) showing IRP2-mediated regulation of ferritin heavy chain (FTH1). Increased iron levels inhibit IRP2, a negative regulator of *FTH1* expression. Immunoblot analysis of FTH1 and SLCO2B1 in indicated human and mouse cell lines expressing vector or *SLCO2B1* cDNA (bottom). β-actin was used as loading control.

(G) Immunoblot analysis of IRP2 and FTH1 in Jurkat and 293T cells expressing vector or SLCO2B1 cDNA, in the absence or presence of iron depleting agents BafA1 (3 nM in Jurkat; 10 nM in 293T), NH_4Cl (1 mM in Jurkat; 5 mM in 293T) or DFO (3 μM in Jurkat; 100 μM in 293T).

(H) Abundance of indicated metals in Jurkat cells expressing vector or *SLCO2B1* cDNA. Results were normalized to total amount of protein and reported as 'pg metal per μg protein'.

(I) Representative bright-field micrographs of *TFRC* knockout Jurkat cells expressing vector, *SLCO2A1* or *SLCO2B1* cDNA. Scale bar is 50 μm.
(J) Fold change in the number (log_2) of *TFRC* knockout Jurkat cells expressing a control vector, *SLCO2A1* or *SLCO2B1* cDNA without (top) or with 0.01 mg/ml ammonium ferric citrate (FAC) supplementation (bottom) after 3 days. (Mean ± SEM, n= 3, Student's t-test, 95% confidence interval). See also Figure S3

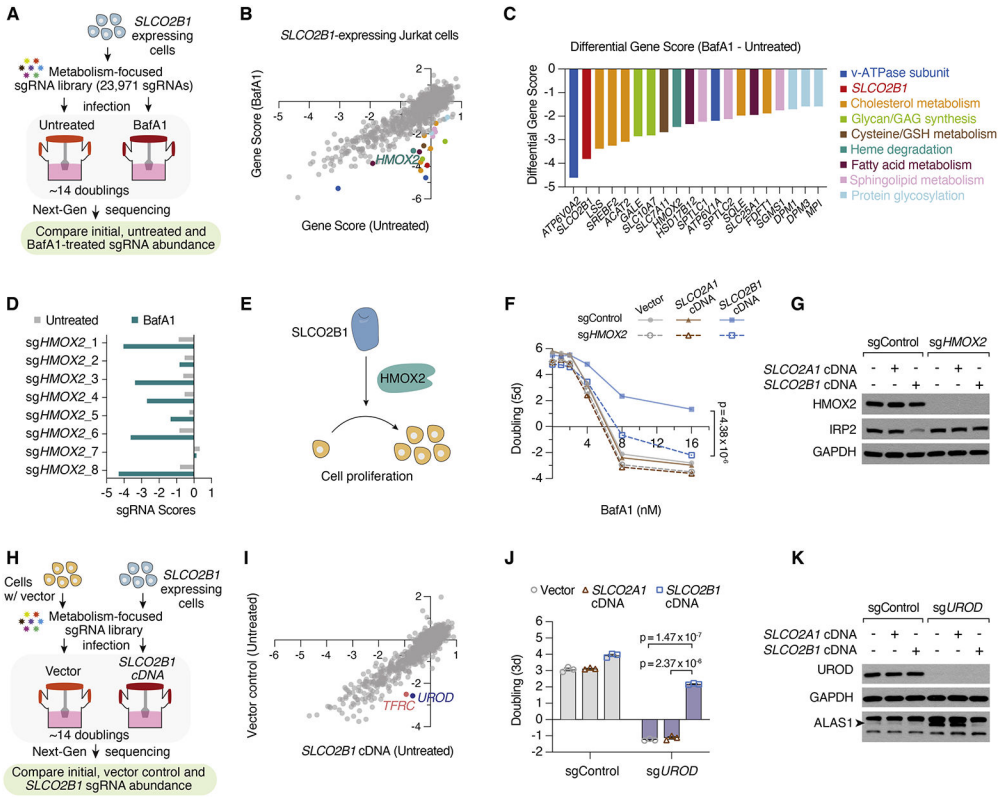

Figure 4. Heme oxygenase is essential for *SLCO2B1*-mediated resistance to iron restriction

(A) Schematic describing CRISPR loss of function screens in Jurkat cells expressing *SLCO2B1* cDNA in the presence and absence of BafA1.

(B) Gene scores of untreated vs. BafA1-treated (4 nM) Jurkat cells expressing *SLCO2B1* cDNA.

(C) Top 20 genes scoring as differentially essential upon BafA1 treatment in *SLCO2B1*-expressing cells compared to vector controls. Differential gene scores are plotted, and color matched with metabolic processes they are involved in, as listed on right.

(D) sgRNA scores of *HMOX2*-targeting sgRNAs in untreated and BafA1-treated Jurkat cells expressing *SLCO2B1* cDNA.

(E) Schematic illustrating the proposed model for SLCO2B1-mediated rescue of cell proliferation under iron restriction.

(F) Fold change in the number (log_2) of control and *HMOX2* knockout Jurkat cells expressing a control vector, *SLCO2A1* or *SLCO2B1* cDNA, during 5-day incubation with or without BafA1 at indicated concentrations. (Mean ± SEM, n= 3, Student's t-test, 95% confidence interval).

(G) Immunoblot analysis for HMOX2 and IRP2 in control and *HMOX2* knockout Jurkat cells expressing vector, *SLCO2A1* or *SLCO2B1* cDNA. GAPDH was used as loading control.

(H) Schematic depicting CRISPR loss of function screen in Jurkat cells expressing a vector control compared to those expressing SLCO2B1 cDNA.

(I) Gene scores of Jurkat cells expressing a control vector or *SLCO2B1* cDNA.

(J) Fold change in the number (log_2) of control and *UROD* knockout Jurkat cells expressing vector, *SLCO2A1* or *SLCO2B1* cDNA after 3 days. Cells were seeded 7 days after infecting with *UROD* sgRNA vector. (Mean ± SEM, n= 3, Student's t-test, 95% confidence interval). (K) Immunoblot analysis for UROD and ALAS1 in Jurkat cells expressing vector, *SLCO2A1* or *SLCO2B1* cDNA infected with a control sgRNA or *UROD* sgRNA. GAPDH was used as loading control. See also Figure S4, Tables S15-S18

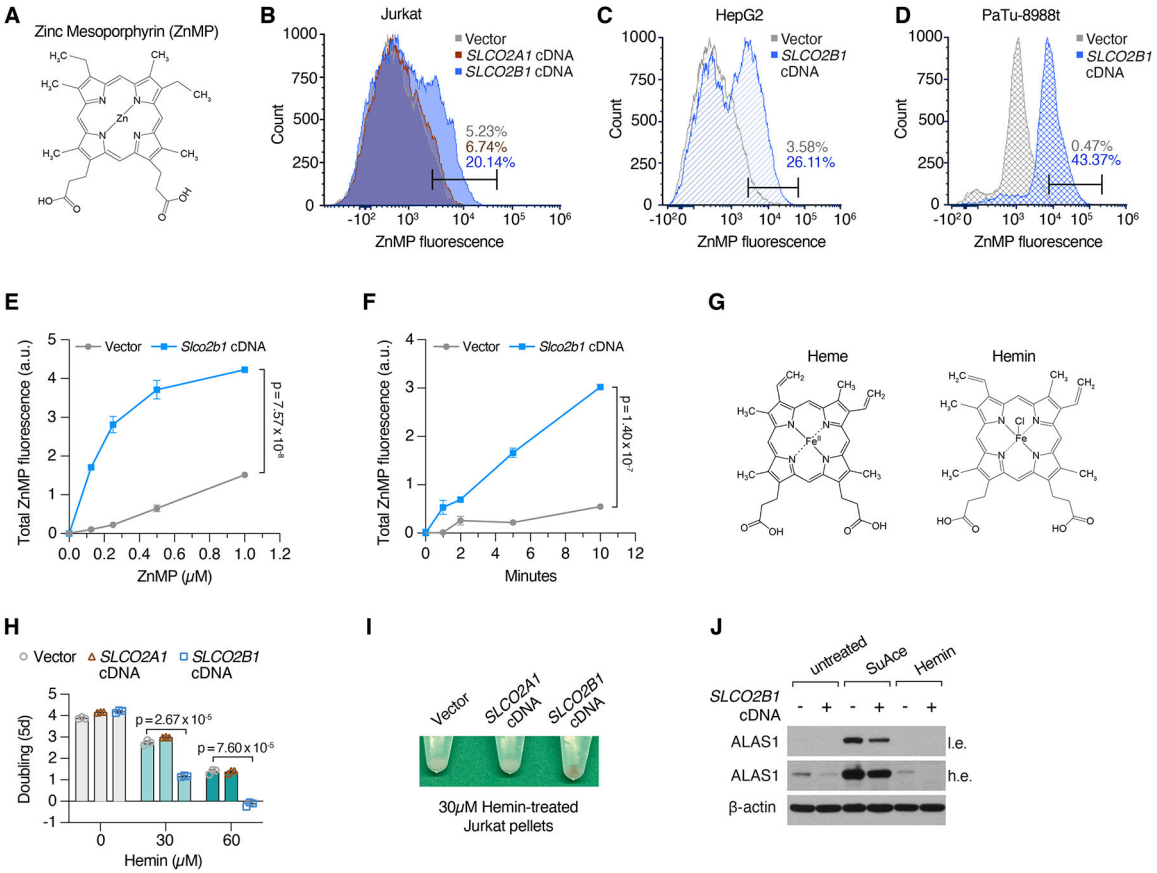

Figure 5. *SLCO2B1* expression is sufficient for the uptake of heme analogs

(A) Chemical structure of Zinc Mesoporphyrin (ZnMP).

(B-D) Flow cytometry analysis of ZnMP uptake in (B) Jurkat cells expressing vector, *SLCO2A1* or *SLCO2B1* cDNA, treated with 5 μM ZnMP for 24 h (C) HepG2 cells expressing vector or *SLCO2B1* cDNA treated with 1 μM ZnMP for 15 min (D) PaTu-8988t cells expressing vector or *SLCO2B1* cDNA treated with 2 μM ZnMP for 15 min.

(E) Dose curve for ZnMP uptake in mouse HY15549 pancreas cells expressing vector or *Slco2b1* cDNA treated with indicated doses of ZnMP for 15 min at room temperature. (Mean ± SEM, n= 3, Student's t-test, 95% confidence interval).

(F) Time course for ZnMP uptake in mouse HY15549 pancreas cells expressing vector or *Slco2b1* cDNA treated with 1 μM ZnMP for the indicated time points.

(G) Chemical structures of Heme B and Hemin.

(H) Fold change in the number (log_2) of Jurkat cells expressing control vector, *SLCO2A1* or *SLCO2B1* cDNA, during 5-day incubation with or without Hemin treatment at indicated concentrations. (Mean ± SEM, n= 3, Student's t-test, 95% confidence interval).

(I) Representative images of cell pellets from Hemin-treated Jurkat cells expressing vector, *SLCO2A1* or *SLCO2B1* cDNA. Cells were treated with 30 μM Hemin for 24 h prior to pelleting.

(J) Immunoblot analysis for ALAS1 in Succinyl Acetone (1mM) or Hemin (30 μM) treated Jurkat cells expressing vector or *SLCO2B1* cDNA. β-actin was used as loading control.

See also Figure S5

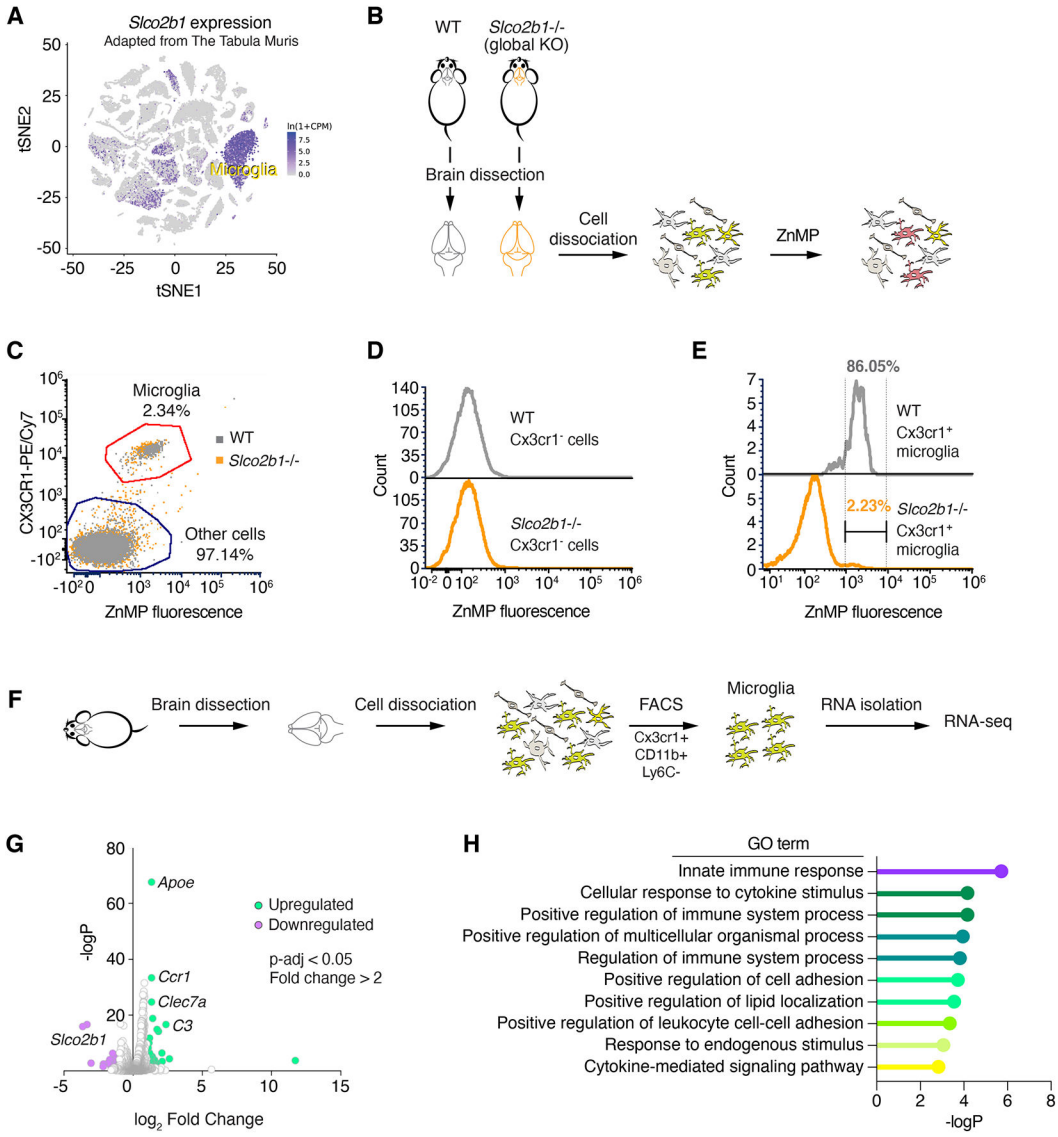

Figure 6. *Slco2b1* is necessary for heme analog uptake in microglial cells

(A) t-SNE plot for *Slco2b1* expression across single cell transcriptome of mouse cell types. Adapted from Tabula Muris.

(B) Experimental strategy for the ZnMP uptake assay of primary cells derived from brains of wild type and *Slco2b1* knockout mice.

(C) Flow cytometry analysis of ZnMP fluorescence and Cx3cr1-labeling (microglia marker) in cells isolated from wild-type and *Slco2b1* knockout mouse brains.

(D) Flow cytometry analysis of ZnMP fluorescence in Cx3cr1^{-} non-microglial cells.

(E) Flow cytometry analysis of ZnMP fluorescence in Cx3cr1^{+} microglia.

(F) Experimental strategy for sorting mouse microglia by FACS for RNA-seq.

(G) Volcano plot for differential gene expression analysis between WT and *Slco2b1−/−* mouse microglia. p-value adjusted <0.05. Upregulated genes (fold change > 2) are shown in green, downregulated (fold change < −2) in purple. See also Table S3.

(H) Gene ontology enrichment analysis for significantly upregulated genes. $p < 0.05$, hypergeometric test.
See also Figure 5

KEY RESOURCES TABLE

REAGENT or RESOURCE	SOURCE	IDENTIFIER
Antibodies		
SLC25A37	Invitrogen	Cat#PA5-26720; RRID:AB_2544220
SLCO2B1	Novus Biologicals	Cat#NBP1-80979; RRID:AB_11038565
Fth1	Cell Signaling Technology	Cat#3998S; RRID:AB_1903974
IRP2	Cell Signaling Technology	Cat#37135S; RRID:AB_2799110
β-Actin	GeneTex	Cat#GTX109639; RRID:AB_1949572
GAPDH	GeneTex	Cat#GTX627408; RRID:AB_11174761
HMOX2	Proteintech	Cat#14817-1-AP; RRID:AB_2118843
UROD	Proteintech	Cat#15547-1-AP; RRID:AB_2213813
ALAS1	Proteintech	Cat#16200-1-AP; RRID:AB_2878227
CRISPR-Cas9	Novus Biologicals	Cat#NBP2-36440; Clone 7A9-3A3
TFRC (CD71)	Cell Signaling Technology	Cat#13113S; RRID:AB_2715594
GFP (for immunofluorescence)	Aves Labs	Cat#GFP-1010; RRID:AB_2307313
GFP (for immunoblotting)	Proteintech	Cat#50430-2-AP; RRID:AB_11042881
Goat anti-Chicken IgY (H+L), Alexa Fluor™ 488	Thermo Fisher Scientific	Cat#A11039; RRID:AB_2534096
Goat anti-Rabbit IgG (H+L), Alexa Fluor™ 555	Thermo Fisher Scientific	Cat#A21428; RRID:AB_2535849
PE/Cy7 anti-mouse CX3CR1 [Clone: SA011F11]	Biolegend	Cat#149015; RRID:AB_2565699
Anti-CD11b Rat Monoclonal Antibody (Brilliant Violet® 711) [clone: M1/70	Biolegend	Cat#101241; RRID:AB_11218791
Anti-Ly-6C Rat Monoclonal Antibody (Brilliant Violet® 510) [clone: HK1.4]	Biolegend	Cat#128033; RRID:AB_2562351
Bacterial and Virus Strains		
NEB Stable Competent *E. coli*	New England Biolabs	C3040
Chemicals, Peptides, and Recombinant Proteins		
RPMI 1640 Culture Media	GIBCO	11875
DMEM Culture Media	GIBCO	11965
Trypsin	GIBCO	25200
Fetal Bovine Serum	Sigma	12306C
Bafilomycin A1	Cayman Chemical	11038
Concanamycin A	Sigma-Aldrich	C9705
Deferoxamine Mesylate	Sigma	D9533
Deferiprone	Selleck Chemicals	S4067
Antimycin A	Sigma-Aldrich	A8674
CB-839	Selleck Chemicals	S7655
Palmitic Acid	Cayman Chemical	10006627
L-Buthionine-sulfoximine	Sigma	B2515
DMSO	AlfaAesar	A13280-36
HPLC Grade Water	Fisher Scientific	W6

REAGENT or RESOURCE	SOURCE	IDENTIFIER
HPLC Grade Methanol	Fisher Scientific	A454-1
Heavy labeled amino acid internal standards	Cambridge Isotopes	MSK-A2-1.2
Ammonium Iron (III) Citrate (FAC)	Sigma	F5879
Ammonium Chloride	Sigma	A9434
Zn(II) Mesoporphyrin IX	Frontier Scientific	M40628
Hemin	Sigma-Aldrich	H9039
Succinylacetone	Cayman Chemical	25501
Ethanol	Fisher Scientific	04-355-222
BsmBI	New England Biolabs	R0580
T4 DNA ligase	New England Biolabs	M0202
ExTaq DNA Polymerase	Takara	RR001A
Hank's Buffered Salt Solution	GIBCO	24020117
XtremeGene9	Roche	6365779001
Polybrene	Sigma	H9268
Puromycin	Sigma	P8833
Blasticidin	Invivogen	ant-bl-1
Critical Commercial Assays		
CellTiter-Glo® Luminescent Cell Viability Assay	Promega	G7571
Deposited Data		
Original western blot images	This work	https://doi.org/10.17632/sg3b3f25p4.1
Experimental Models: Cell Lines		
Jurkat	ATCC	TIB-152
HepG2	ATCC	HB-8065
MDA-MB-231	ATCC	CRM-HTB-26
HEK293T	ATCC	CRL-1573
PaTu-8988t	Dr. Monther Abu-Remaileh (Stanford University)	N/A
AK196	Dr. Haoqiang Yang (MD Anderson Cancer Center)	N/A
HY15549	Dr. Nabeel El-Bardeesy (Massachusetts General Hospital Cancer Center)	N/A
4T1	Dr. Sohail Tavazoie (Rockefeller University)	N/A
4T07	Dr. Sohail Tavazoie (Rockefeller University)	N/A
Experimental Models: Organisms/Strains		
C57BL/6N-Slco2b1$^{tm1a(KOMP)Wtsi}$/Mmucd	Mutant Mouse Resource and Research Center (MMRRC)	049765-UCD
C57BL/6J	The Jackson Laboratory	000664
Oligonucleotides		
DNA oligonucleotides and primers	This study	See Table S19
Recombinant DNA		

REAGENT or RESOURCE	SOURCE	IDENTIFIER
pLV-EF1a-IRES-Blast	Addgene	85133
plentiCRISPR puro v2	Addgene	52961
lentiGuide Puro	Addgene	52963
CRISPRa dCas9-VPR vector with hEF1a promoter	Horizon Discovery	CAS11916
pLV-EF1a-IRES-Blast_SLC25A37	This study	N/A
pLV-EF1a-IRES-Blast_SLCO2B1	This study	N/A
pLV-EF1a-IRES-Blast_SLCO2B1 (short isoform)	This study	N/A
pLV-EF1a-IRES-Blast_SLCO2B1-eGFP	This study	N/A
pLV-EF1a-IRES-Blast_SLCO2A1	This study	N/A
pLV-EF1a-IRES-Blast_SLCO2A1-eGFP	This study	N/A
pLV-EF1a-IRES-Blast_Slco2b1 (mouse cDNA)	This study	N/A
plentiCRISPR puro v2_sgTFRC_1	This study	N/A
plentiCRISPR puro v2_sgUROD_1	This study	N/A
plentiCRISPR puro v2_sgUROD_2	This study	N/A
plentiCRISPR puro v2_sgHMOX2_1	This study	N/A
Human metabolism-focused CRISPRa sgRNA library	This study	N/A
Mouse metabolism-focused CRISPRa sgRNA library	This study	N/A
Metabolism-focused sgRNA library	Birsoy et al., 2015	N/A
Software and Algorithms		
XCaliburQual Browser 2.2	ThermoFisher	https://www.thermofisher.com/order/catalog/product/OPTON-30965#/OPTON-30965; RRID: SCR_014593
Skyline Daily	MacCoss Lab	https://skyline.ms/project/home/software/Skyline/begin.view; RRID: SCR_014080
FCS Express 7	DeNovo Software	https://denovosoftware.com/; RRID: SCR_016431
Prism 9	GraphPad	https://www.graphpad.com/scientific-software/prism/; RRID: SCR_002798
Other		
Z2 Coulter Counter	Beckman	Model Z2
SpectraMax Microplate Reader	Molecular Devices	Model M5
Primovert Microscpe	Carl Zeiss	415510-1105-000
FACSAriaII	BD Biosciences	643181
Multiphoton microscope with confocal modality	Nikon	A1R MP